Paper No.
13076

NACE INTERNATIONAL
CORROSION Conference & Expo 2019

Modelling the Effect of Porous Iron Sulfide Layers on Sour Corrosion Behaviour

J. Amri, J. Kvarekvål, M. Tjelta
Institute for Energy Technology
P.O. Box 40, N-2027 Kjeller, Norway

ABSTRACT

Surface layers and deposits of iron sulfides formed from sour corrosion may exhibit both protective and corrosive properties, depending on the types of iron sulfide formed and the physical structure of the layers. The protective barrier and blocking effects of the layers may be counteracted by significant cathodic activity on the surfaces of electrically conductive iron sulfides and galvanic corrosion of the underlying steel surface. Experimental and modelling work were performed to quantify the effects that parameters such as layer thickness and porosity, H_2S partial pressure, temperature and pH can have on the electrochemical reactions, aqueous equilibria and mass-transport processes governing the corrosion rate. The results were discussed in the light of available literature and compared to relevant sour corrosion data, including both native corrosion product layers and applied iron sulfide deposits (UDC).

Key words: sour corrosion, under-deposit corrosion, galvanic corrosion, H_2S, iron sulphide

INTRODUCTION

The occurrence of under-deposit corrosion, commonly referred to as UDC, is mainly confined to stagnant or low-flow regions of production and transmission lines, wherein the local conditions are favourable for either the build-up of surface deposits or the formation of corrosion films [(1)]. Corrosion deposits are, however, commonly observed, even in circulating corrosive media practically devoid of corrosion products [(2)]. Owing to the inherent difficulty to probe, monitor and control such a type of corrosion, the UDC has been identified by the petroleum actors as an extremely insidious scenario, particularly ubiquitous in sour oil and gas fields. Such a scenario can lead to costly failures for the petroleum industry, where the safety, technical, and economic stakes are high. The situation might indeed be awkward for mitigation and pigging, as the use of traditional inhibitors might have little or no impact on the corrosion process in the presence of surface deposits [(3)]. These, indeed, might behave as a barrier to the surfactant inhibitor, and might

prevent it from reaching - with the required dose rate - the metal surface meant to be protected. The question of how solid deposits affect the efficiency of corrosion inhibitors has been extensively addressed in literature, with sometimes antagonistic explanations.

In the present work, the effect of established surface deposits, both reacting and insulating, on sour corrosion has been modelled using the COMSOL Multiphysics platform†. The modelling effort aimed at gaining insights of characteristic features of the UDC both with and without galvanic activity, and bridging the gap between the experimental findings thus far. It also paved the way for the prediction of the impact of a range of variables, thus helping to provide a fairly clear picture of this form of corrosion, with the emphasis on porous reacting Fe_mS_n layers.

FIELD AND LABORATORY EXPERIENCE

In H_2S environments, field observations show that Fe_mS_n films can be very protective for long periods of time, but there are also several reports of corrosion failure [4]. The dynamics of UDC is highly impacted by the nature of the porous deposits, as well as their physicochemical behavior. The degree of UDC is further exacerbated due the intrinsic electrical properties of iron sulfides, which were found to be conductive regardless of their polymorphism [5]. These latter are even often pointed at as potential cathodic surfaces. A good electrical connection between the deposit and the host surface, along with a fairly low IR drop throughout the supporting electrolyte are generally favorable conditions for the onset of UDC, whose extent is commonly boosted in the presence of extraneous contributors. These are typically anodic promoters such as sulfur, oxygen and bacteria. Besides the materials dissimilarity between the Fe_mS_n layers and the host surface, geometric constraints often result in restrictions of local exchange of matter. Uneven mass-transfer between adjacent areas at various positions along the metal surface might yield a local chemical differentiation, thus favouring localized galvanic corrosion. Once the occluded environment is set up beneath the deposit, the metal dissolution might be confined to tiny anodic islets, thereby resulting on a large ratio of cathodic-to-anodic areas. The cathodic reactions might be progressively delocated on the external surface of the deposit in contact with the bulk environment, where the inward diffusion of cathodic reactants through the porous structure is no longer a rate limiting step, the deposit being presumed here to be electroactive. All these factors combined are likely to increase the dissolution rate to one extent or another and, worse still, trigger, drive, and make the pitting corrosion autocatalytic. The overall process is hence a scenario that involves a complex interplay of mass-transport, heterogeneous electrochemical reactions and solution chemistry. It could be interpreted as three competing mechanisms involving *(i)* dissolution, and thus production of precipitable species; *(ii)* precipitation kinetics and film formation; and finally *(iii)* local mass-transport, and replenishment of the constrained medium from the bulk solution.

A large body of literature [5] exists which deal chiefly with the general corrosion of steel under various sour conditions. While most of such studies has been dedicated to the understanding of the chemical and thermodynamic properties of iron sulfides, little attention has however been paid to their electrochemical properties. Several models have also been proposed for the prediction of the general corrosion rate in sour environments, although none deal specifically with corrosion in the presence of surface deposits. The contributions of reacting Fe_mS_n deposits and Fe_mS_n corrosion films to sour UDC, and whether these two types of surface layers behave analogously, are, however, still subject to controversy. The nascent models and experimental data reported in literature are overall not satisfactory enough to provide a clear depiction of the sour corrosion mechanism beneath a stabilized surface deposit. Also, the complexity of these surface conditions

† Trade name.

makes them quite difficult to reproduce [2], and laboratory simulations and measurements are rarely reminiscent of the genuine behaviour of UDC, not to mention here that deposits obtained in the laboratory are often not the same as those observed in real situations. Because of all these experimentally quasi-inextricable difficulties enacted by a complex interplay of solution chemistry, mass transport, and heterogeneous electrochemical processes, the modelling of UDC proves to be an obvious topic of interest to the corrosion community in the oil and gas industry.

The detrimental effect of porous iron sulfide deposits is illustrated in Figure 1, in which corrosion test coupons exposed with and without a pre-applied layer of FeS powder are compared. The weight loss corrosion rates were around 1 mm/y without and 10 mm/y with deposited FeS. Also, as indicated by the 3D profiles, localized corrosion (wide and narrow pitting) took place on the UDC coupon. This example is taken from a previous report on the effect of iron sulfide deposits on sour corrosion. [3]

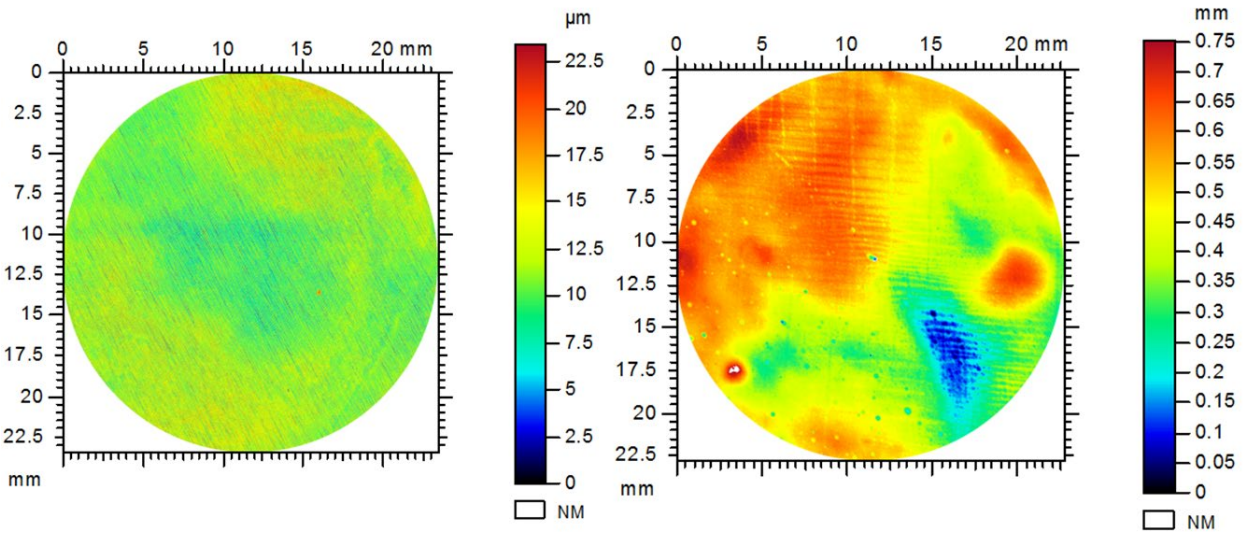

Figure 1: Comparison of 3D profiles of regular (left) and under-deposit corrosion (right) test coupons exposed to H_2S/CO_2-saturated brine. Test conditions: 25°C, 10 bar H_2S, 10 bar CO_2, 100g/L NaCl, 10 mmol/L added alkalinity, duration 14 days. Deposit on UDC coupon: FeS, ca 1 g/cm^2. [3]

MODEL DESCRIPTION

Tracking the electrochemical behaviour of porous reacting Fe_mS_n layers, whose effects were contrasted to those observed in the presence of insulating deposits (*e.g.* sand; clay), was the focus of the present modelling effort. The modelling workflow encompasses the aqueous chemical and electrochemical reactions of the H_2S/H_2O/Fe system on a corroding steel surface covered with a porous deposit/corrosion layer, as well as the exchange of matter and hydrodynamic conditions. The physical description is divided into the following sections: *(i)* summary of the assumptions, *(ii)* description of the modeled regions, *(iii)* governing equations and assumptions for each region, and finally *(iv)* boundary conditions. For the sake of brevity, the abbreviations "*PRL*" and "*PIL*" are used hereafter with reference to a *porous reacting layer*, and a *porous insulating layer*, respectively.

Summary of assumptions

Simplifying, but otherwise appropriate assumptions were introduced in order to scale the mathematics down to a workable level, with a physical description as less cumbersome as possible, while ascertaining that equations are still consistent and do not obviate the true behaviour of the porous structure. The mathematical depiction of the underlying physics was cast in terms of variables customarily resorted to in porous electrode theory, with a Nernst-Planck formalism. The major assumptions adopted in the development of the present model are the following: one spatial coordinate (*x*); steady state; dilute solution theory; no heterogeneous reactions; smooth interface (Fe_mS_n films) and particles (Fe_mS_n deposits); no structural changes of the porous layer; no potential drop within the solid phases.

Description of the modeled regions

A one-dimensional schematic representation of the system under investigation, as well as the physico-chemical processes pertaining to each region are depicted in **Figure 2**, with *x* having its origin at the porous layer-metal interface. The two modeled regions of interest are the porous layer (δ_f), and the diffusion layer (δ_d - δ_f) that adjoins the free electrolyte.

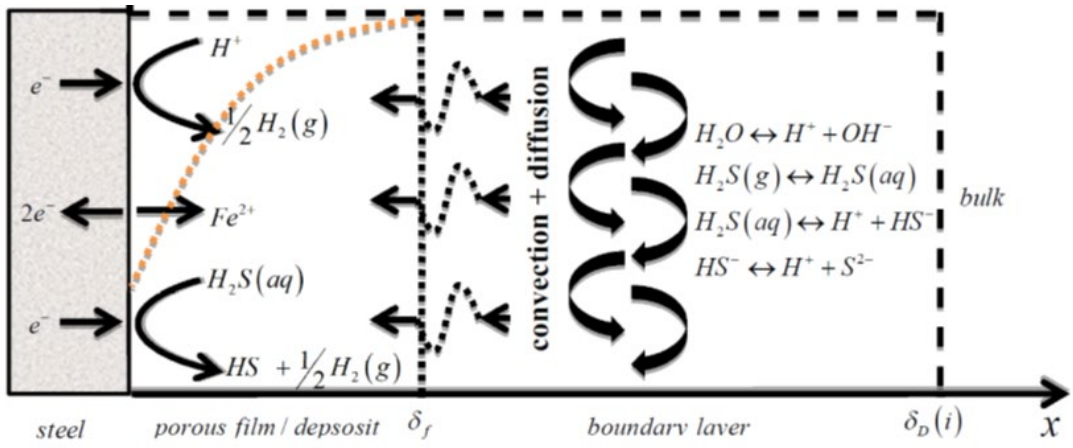

Figure 2: Schematic view of the modeled regions. The dotted orange curve depicts the hypothetical porosity whose fluctuation in space and in time was however disregarded in the present model, and will be addressed in future work.

Diffusion layer

Across the natural diffusion layer, species owe their motion in solution to their diffusion in an electric field supplemented by forced convection, *viz.* a combination of “chemical” diffusion, convection, and electromigration for ionic species. The concentration per unit volume of electrolyte of dissolved species is governed by the material balance. At steady state, the differential conservation law yields:

$$\frac{\partial C_i}{\partial t} = 0 = -\frac{\partial N_i}{\partial x} + R_i \qquad (1)$$

The R_i term denotes here the production rate of species i by homogeneous chemical reactions. The condition of electroneutrality is also used as the governing equation for the electrolyte potential, that is, $\Sigma z_i C_i = 0$ at any $x \geq \delta_f$. The present model involves six species. These are: H^+, OH^-, $H_2S_{(aq)}$, HS^-, S^{2-}, Fe^{2+}.

Porous layer

In general, in the physical model, the microscopic description of a porous layer would consist in considering that all happens as if the pores are so interlinked so that the porous structure would behave as a uniform system [6]. In the present model, the porous layer is assumed to be fully saturated with a strongly supported electrolyte (flooded structure); any accumulation of gaseous bubbles within the pore structure is not permitted whatsoever. In the case of *PRL*s, it is deemed appropriate to treat the porous region as a smooth structure, whose reacting surface area is mostly internal [7]. The total porosity is divided into accessible and non-accessible porosities, that is, $\varepsilon_t = \varepsilon_a + \varepsilon_{na}$. The non-accessible porosity includes isolated pores and inter-particle spaces. These isolated pores are physically too small for diffusing species to percolate their tiny structures. Also, eventual solutes and reactions occurring within non-accessible pores have in general no influence on the caustic environment [8]. Only the accessible porosity will hence be considered further here. The accessible porosity, which refers to all the connected through and dead-end pores, is in turn divided into an effective porosity (connected through-pores) and a storage porosity (blind pores), that is, $\varepsilon_a = \varepsilon_e + \varepsilon_s$. In the following, it is assumed that the porous layer is mainly made of connected through-pores, so that ε_a and ε_e can be used interchangeably; either one is simply referred to by ε. For a particulate *PRL*, the total perimeter area of the macroporosity, corresponds to the area through which mass-transport to the reacting surfaces can occur. The specific surface area S_m ($cm^2.cm^{-3}$), associated with this latter area, is inversely proportional to the particle diameter. This area may be equated to the total specific surface area for reaction, S_a ($cm^2.cm^{-3}$), with the assumption of smooth particles, *i.e.* devoid of microporosity (roughness factor, $f_r = 1$). Recall that the total specific surface area is, in theory, S_m times the roughness factor (*i.e.* $S_a = f_r.S_m$), with f_r referring to all the area associated with unit geometric macroporous area [6]. In order to anticipate any asymmetry and anisotropy over the length scale of local transport within the porous reacting structure, the statement of mass-conservation pertaining to the porous medium is formulated in terms of average quantities. In this way, averaging is applied to a finite volume element throughout the porous medium, and details on the length scale of transport at the level of small active material particles are astutely coupled to the volume averaged transport over much larger length scales. For the sake of simplicity, the pore structure is described without regard to its actual geometric details. Average quantities are hence defined using the effective transport properties of the porous medium, adjusted by the macroscopic parameters, *viz.* the porosity (ε), and the tortuosity (τ). These are interrelated through a dimensionless parameter, usually referred to as the MacMullin number, $N_{mac} = \tau/\varepsilon$. A simple, yet powerful, estimation for tortuosity is the Bruggeman relation, $\tau = \varepsilon^{\alpha}$, with α the Bruggeman's exponent, being commonly set to - 0.5. Within the porous layer, the flux of species i, is defined per unit exposed area of the porous structure. In addition to the foregoing R_i term, the steady-state mass-transport balance pertaining to the volume averaged transport within the *PRL* shall hence entail a pseudo-homogeneous reaction rate term, noted hereafter R_i'.

$$\frac{\partial(\varepsilon C_i)}{\partial t} = 0 = -\frac{\partial N_i}{\partial x} + \varepsilon R_i + R_i' \qquad (2)$$

It stands for the production rate of species i due to all of the electrochemical reactions that it may be involved in within the porous reacting matrix. Similar to the diffusion layer region, the requirement for electroneutrality was also assumed to hold for the porous medium, that is, $\Sigma z_i C_i = 0$ at any $x \leq \delta_f$. It should be borne in mind that the εC_i term refers to the superficial concentration, *viz.* the average concentration per total unit volume of the porous medium, including the solid matrix and the pore-filling electrolyte.

Boundary conditions

With D_{H+} being the largest diffusion coefficient out of all of the species considered, the thickness $\delta_d(H^+)$ naturally emerges as the best appropriate scale of reference for the bulk conditions, *viz.* $C_i\ (\delta_d) = C_i\ (bulk)$. Beside the dissolution of the underlying metal, all the cathodic reactions were enabled at $x=0$. The molar fluxes of electroactive species are proportional to the local partial current densities, j_k. The sulfide ions S^{2-} are electrochemically non-electroactive in the steady state, and are hence fluxless at the solid-electrolyte interface. The fluxes of inert species, in this case Na^+ and Cl^-, also cancel out. In the present model, the dissolution of iron was assumed to be a one-step process and activation-controlled.

$$N_i\big|_{x=0} = -\varepsilon \sum_k \frac{\nu_{ik} j_k}{n_k F} \tag{3}$$

During corrosion of the metal beneath the porous structure, the cathodic and anodic reactions are in dynamic equilibrium. These partial reactions evolve at rates whose range depends upon the potential difference across the active interface between the solid phase and the electrolyte. At a given position along the active surface, the local overpotential (η_k) is defined as being the difference between the potential of the solid phase (φ_s), arbitrarily taken to be zero, and the electrolyte potential (φ_e) measured against the equilibrium potential $E_{eq,k}$ for reaction k. That is:

$$\eta_k = \varphi_s - \varphi_e - E_{eq,k} \quad ; s \in \{m; PRL\} \tag{4}$$

The production rate of electroactive species i due to all of the NR electrochemical reactions within the *PRL* is given by [7, 9]:

$$R_i' = -\sum_k^{NR} \frac{\nu_{ik} S_a j_{k,c}}{n_k F} \tag{5}$$

with S_a referring to the internal active specific surface area of the porous matrix. The $j_{k,c}$ term is the local current density due to the cathodic reaction $k \in [1, NR]$ occurring on the electroactive surface area within the porous layer. Recall that the $S_a.j_{k,c}$ term is none other than the local volume average current density, referred to hereafter as $j_{k,v}$ in units of $A.m^{-3}$. Over the range of interest, the *current vs. potential* behavior, both within the porous reacting matrix and at the metal surface underneath, was derived by expressing the electrochemical reactions in forms of Butler-Volmer rate expressions with consideration of mass-transport limitations. To the extent possible, literature values of the respective exchange current densities were used to obtain the values of kinetic parameters. Additional values were also obtained by correlating the calculated *current vs. potential* curves to experimental results. It is worth pointing out that the R_i' term vanishes for a *PIL*, and its contribution must therefore be ruled out from the mass balance pertaining to the

porous layer region. The bulk and boundary conditions relative to each specie considered are summarized in **Table 1**.

Table 1
Synopsis of the bulk and boundary conditions.
(*) Not applicable for porous insulating layers (PIL).

	x	OH^-	Fe^{2+}	H^+	$H_2S_{(aq)}$	HS^-	S^{2-}
Domain							
Bulk solution	$x \geq \delta_d(H^+)$	Equilibrium reactions					
Porous layer	$0 < x \leq \delta_f$						
Boundary conditions							
Metal	$x = 0$	-	Anodic reaction	Cathodic reactions			0
Porous layer	$0 < x \leq \delta_f$	-	-	Porous electrode cathodic reactions (*)			-
Bulk solution	$x = \delta_d(H^+)$	Bulk equilibrium concentrations, $C_{i,\ bulk}$					

The model presented forth above is described by a set of differential equations associated with six unknowns, C_i, and one nonlinear equation for the requirement of electroneutrality, with φ_e being the unknown variable. These equations, along with their proper boundary conditions, were solved numerically for the concentration and potential profiles throughout the two modeled regions. The input variables to the model include the temperature (T_C); the composition of the gas phase (pH_2S); the composition of the bulk electrolyte (pH_{bulk}; $C_{0,Fe2+}$); the morphology properties of the porous layer (δ_f; ε; S_a); and the hydrodynamic condition (Ω_{rpm}). The supporting electrolyte consisted of anaerobic 100 $g.L^{-1}$ NaCl solutions, pre-saturated with 10 bars $H_2S_{(g)}$, and initially free of Fe^{2+} cations. For a pure matter of convergence, however, the initial concentration of Fe^{2+} cations in the bulk was set to 10^{-5} M, that is, far below the mean level of saturation threshold of iron. The values of the input variables reported in **Table 2** were used as the baseline conditions when varying the different parameters, one at a time. The reference value adopted for porosity for either case (*PIL*; *PRL*) was 38%, which is thought of as akin to the porosity of poured sand.

Table 2
Baseline conditions.

Input variable		**Value**
pH_2S	Pressure of H_2S in the gas phase	10 bars
pH_{bulk}	pH in the bulk electrolyte	3.66
T_C	Temperature	25 °C
ε	Porosity	0.38
Ω_{rpm}	Rotation speed	100 rpm
δ_f	Thickness of the porous layer	1 mm

The model was implemented in a finite element platform, namely COMSOL Multiphysics®, and predictions were generated for porous reacting Fe_mS_n layers (*PRL*; *scenario* I), whose effects were contrasted to those of inert deposits with no galvanic activity, such as sand and clays (*PIL*; *scenario* II). The assumption of uniform morphology of the Fe_mS_n layers entails here that the latter are not corroding. Also, any accumulation of the corrosion products, either within the porous layer or on the top of its outer surface, would thereby yield a change in the layer form and hence its nature. Such transient structural variations are nevertheless not accounted for in the present model. When reacting, however, Fe_mS_n layers offer a supplementary reactive surface area for the cathodic reactions considered; these also proceed on the underlying metal in both scenarios, albeit at different rates. The model does not however require *a priori* specification of where the anodic and cathodic reactions occur along the metal surface; their respective locations and rates are instead determined by the local potential distribution.

Throughout all of this, it should be borne in mind that in all cases, Fe^{2+} cations involved in the material balance are provided solely by the iron discharged into solution by the corrosion of the metallic substrate. Also, all the calculations were performed at the free corrosion potential E_{corr} proper to each case, and no external voltage was therefore applied to the system. All the values of E_{corr} reported hereafter are referred to a silver chloride electrode.

RESULTS AND DISCUSSION

When combined to the effect of the operating conditions, the disparity between the two solid phases in terms of intrinsic conductivity, electroactive surface area, and electrocatalytic activity would create a wide spectrum of influence by the porous layer on the corrosion rates of the host metal. It would therefore be cumbersome to report detailed parameter studies for every possible case. In as far as the present model is preliminary in nature, only a few representative results of special interest have been presented and discussed hereafter.

Typical concentration profiles at the corrosion potential throughout the two modelled regions are illustrated in **Figure 3**. These C_i *vs.* x plots were generated for the two scenarios at the reference conditions of **Table 2**. For visual convenience, the concentrations are displayed on a logarithmic scale. At equilibrium, and at $x = \delta_d$, the concentration profile of each specie considered attains a constant value, which is none other than the concentration at the bulk phase. The continuity condition between the two regions implies, *a priori,* that the flux of each species must be continuous across their common interface. This requirement is accommodated by the change of the concentration gradients at $x = \delta_f$. Also, in order to compensate for a smaller diffusion coefficient within the porous layer ($D_{i,e} = D_i/N_{mac} = \varepsilon^{1.5} \times D_i$), the concentration gradient of a given species at $x = \delta_f^-$ must be larger than at $x = \delta_f^+$.

A straightforward comparison between the two scenarios shows that the depletion both in H^+ and $H_2S_{(aq)}$ is even more marked further inwards when the porous layer is reactive. While a *PIL* is expected to provide only a physical barrier to mass-transport, a *PRL*, in contrast, confers a larger surface area, as defined by a larger specific surface area S_a, thereby yielding higher reduction rates of the cathodic reactants. For a sake of clarity, the concentration profiles of $H_2S_{(aq)}$ and H^+ (pH) are shown separately in **Figure 4 (a)** and **Figure 4 (b)**, respectively.

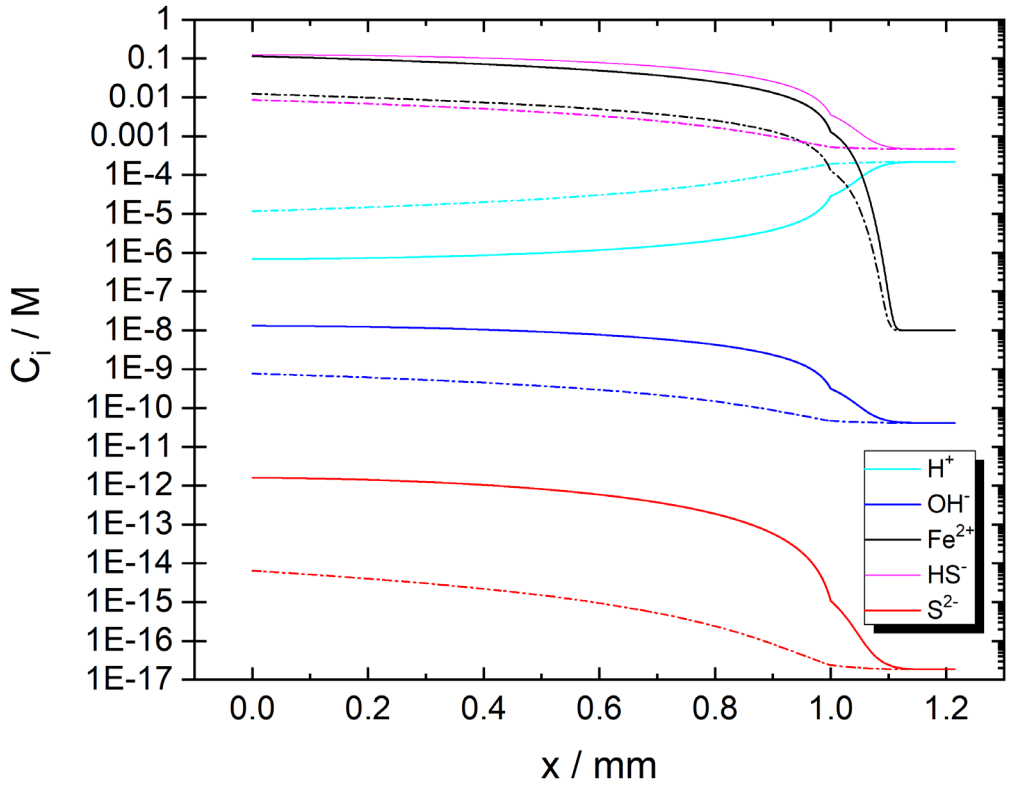

Figure 3: Typical C_i vs. x profiles within a porous Fe_mS_n layer at the reference values of Table 2. The solid lines denote scenario I (reacting Fe_mS_n layers), and the dash-dotted, scenario II (insulating Fe_mS_n layers).

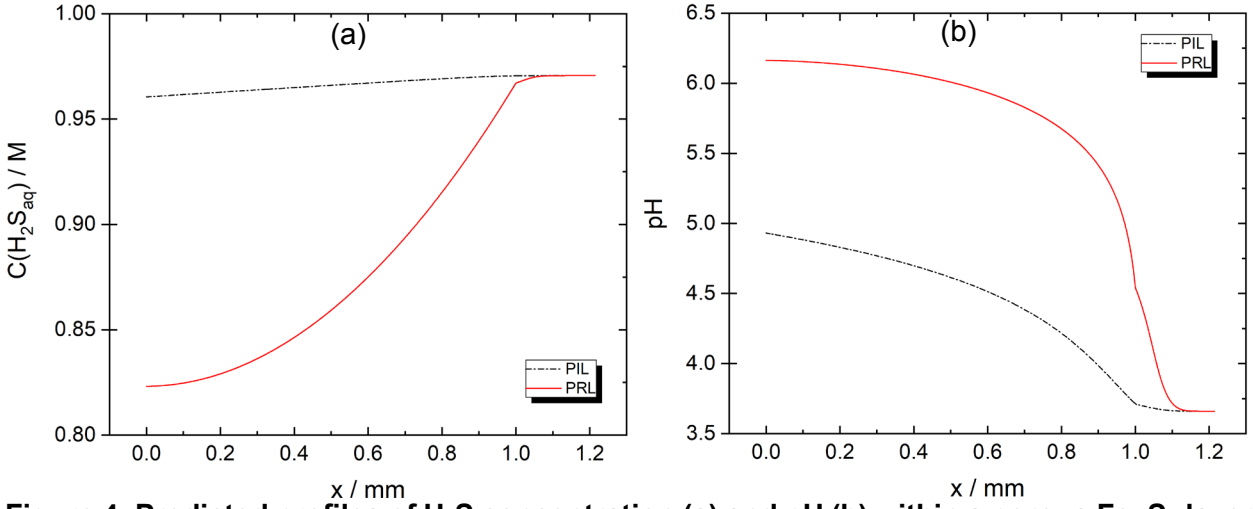

Figure 4: Predicted profiles of H_2S concentration (a) and pH (b) within a porous Fe_mS_n layer at the reference values of Table 2. PIL= porous insulating layer, PRL= porous reacting layer.

The progressive exhaustion of H^+ and $H_2S_{(aq)}$ and the enrichment in Fe^{2+} within the porous layer is likely to yield a transition towards more saline and less acid cases. The simulation results show that this transition is even more accelerated in the presence of porous reacting Fe_mS_n layers. Due to an enhanced reduction of $H_2S_{(aq)}$, the rise in HS^- concentration further inwards becomes even

more pronounced when the porous Fe_mS_n layer is reactive. Recall that the bisulfide anions, are produced both chemically via the dissociation reaction of $H_2S_{(aq)}$, and electrochemically via the direct reduction of $H_2S_{(aq)}$ on the underlying metal, as well as throughout the porous layer when this latter is reactive. Besides the local pH, the production of HS^- are hence expected to be strongly influenced by the distribution of $H_2S_{(aq)}$ reduction reaction within the porous layer, i.e. $\nabla(-F.\sum_i z_i.N_i)$. Predications also show that S^{2-} ions are present in minute amounts, so that their participation in eventual mechanisms of formation of new solid phases is either unlikely or marginal at this stage. Consequently, only $H_2S_{(aq)}$ and HS^- species emerge as better candidates for such mechanisms. In principle, once the saturating iron concentration is exceeded, the precipitation of new corrosion products within the occluded medium wouldl be triggered on the rear face of the porous structure where the concentration is highest, i.e. on the uncovered areas of the underlying metal. Structural variations due to the formation or precipitation of new Fe_mS_n solid phases, were however disregarded in the present model and will be addressed in a future work.

At the reference conditions of **Table 2**, the corrosion rates were roughly estimated to 0.54 mm/year for inert deposits and 5.46 mm/year for active Fe_xS_y layers. The corrosion potentials were respectively estimated to – 641.4 mV/Ag-AgCl (inert) and – 493.8 mV/Ag-AgCl (active). Typical profiles of the electrolyte potential (φ_e) within the two porous layers are depicted in **Figure 5**. The simulation results also showed a progressive delocalization of the cathodic activity towards the boldly exposed surface. This delocalization stems, *a fortiori*, from an outward depletion of the oxidizing species within the porous structure.

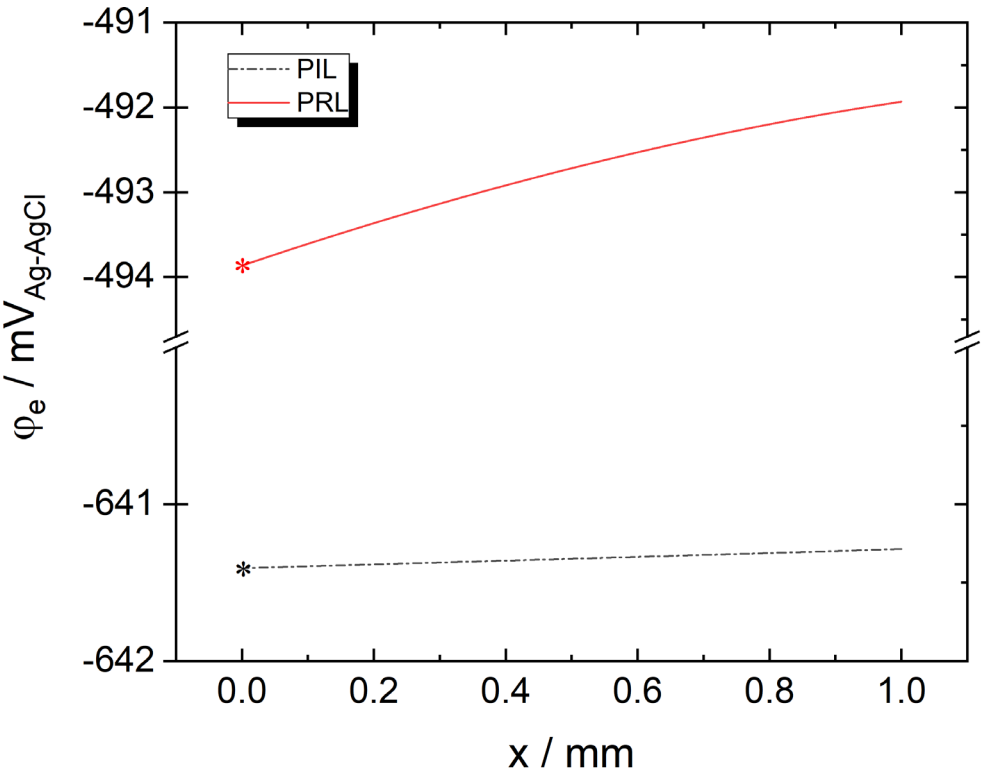

Figure 5. Predicted distributions of the electrolyte potential (φ_e) within a porous Fe_mS_n layer at the reference values of Table 2. The asterisk markers to the leftmost side denote the respective E_{corr} values of the underlying metal. PIL= porous insulating layer, PRL= porous reacting layer.

The average superficial current density for a given reaction k∈[1, NR], hereafter referred to by $j_{k,av}$, is defined as the current density divided by the projected planar (geometric) area of the *PRL*. A value for $j_{k,av}$ can be calculated by integrating the local volume average current density $j_{k,v}$ over the thickness of the porous layer.

$$j_{k,av} = \int_{x=0}^{x=\delta_f} \left(S_a j_{k,c}\right) dx = \int_{x=0}^{x=\delta_f} j_{k,v} dx \qquad (6)$$

The total average superficial current density pertaining to the *PRL* can then be found by summing the superficial current densities due to the individual cathodic reactions, that is, $j_{T,av} = \sum^{NR} j_{k,av}$. Since these reactions also proceed on the metal surface, the total cathodic current density is thereby the sum of $j_{T,av}$, and the total cathodic current density relative to the backing surface (m).

$$j_{T,c} = j_{T,av} + \sum_{k=1}^{NR} \left(j_{k,c}\right)_m = j_{T,av} + j_{T,m} \qquad (7)$$

At the reference conditions of **Table 2** and the mixed potential, a total anodic current density of $j_{Fe2+} \approx 12.35\ A.m^{-2}$ was recorded on the metal surface. At the same conditions, the total cathodic current density on the metal was $j_{T,m} \approx -0.06\ A.m^{-2}$, whereas the total average superficial current density relative to the *PRL* was $j_{T,av} \approx -12.29\ A.m^{-2}$. Using Eq. (7), the total cathodic current density is found $j_{T,c} \approx -12.35\ A.m^{-2} = -j_{Fe2+}$. During corrosion of the underlying metal, no net current density is therefore flowing along the active surface, and the rate of iron oxidation is equal to the total rate of cathodic reactions, that is, $j_{T,c} + j_{Fe2+} = 0$.

The distributions of the partial current densities across a porous reacting Fe_mS_n layer at the reference conditions are depicted in **Figure 6**. The total cathodic current density was referred to by the dotted line. The figure shows that the reduction reaction of water is marginal as expected (blue line). Most of the cathodic activity within the *PRL* was found to be related to the reduction of $H_2S_{(aq)}$. Unlike H^+, the simulation results showed that the reduction rate of $H_2S_{(aq)}$ is quasi-constant across the porous structure. Also, the reduction of H^+ occurs mainly towards the external surface, where protons are more available.

The variation of the corrosion rate with porosity is presented in **Figure 7**. In the presence of active Fe_mS_n layers, the corrosion rate was found to increase with porosity until the latter reaches a critical value. Further increase of the porosity beyond this critical value results in a decline of the corrosion rate. The existence of this maximum stems from the counteracting actions of mass transport and cathodic activity (active specific area). A different behaviour was however found in the presence of inert deposits, where the corrosion rate was shown to increase very slightly with porosity. A more open structure is indeed less restrictive to mass transport of the oxidizing species from the bulk towards the corroding substrate.

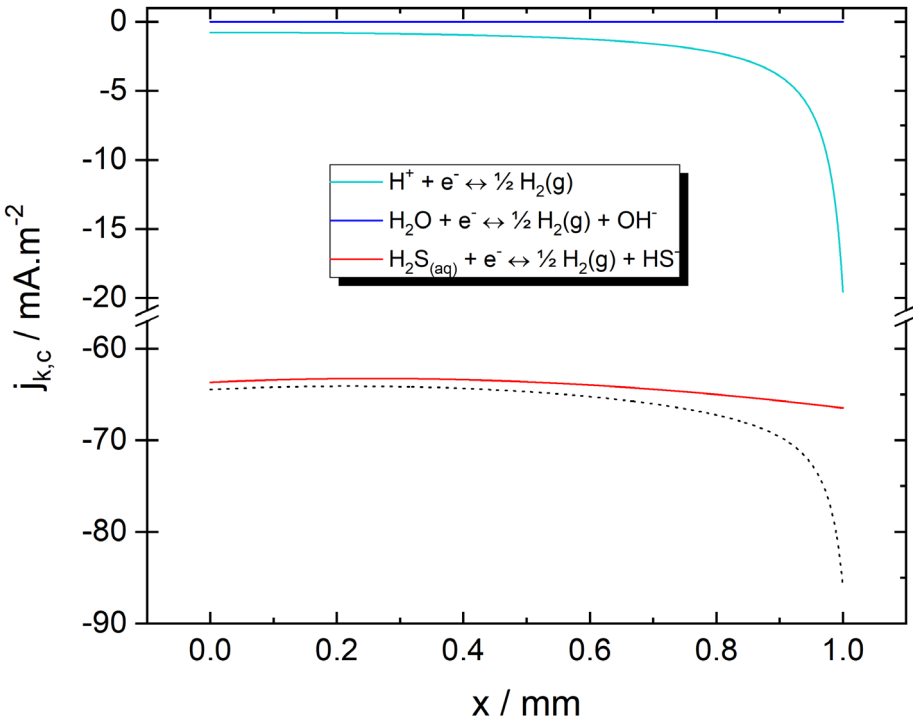

Figure 6. Predicted distributions of the partial cathodic current densities within a porous reacting Fe_mS_n layer at the reference values of Table 2. The dotted line denotes the distribution of the total cathodic current density obtained by summing the individual $j_{k,c}$ terms.

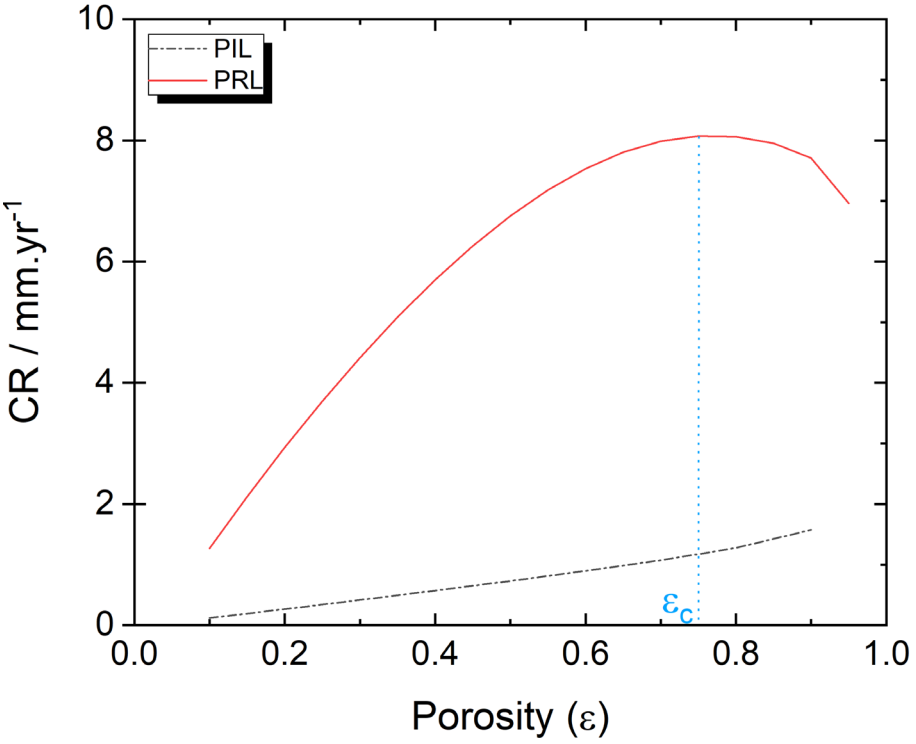

Figure 7. Predicted variations of the corrosion rate with porosity at the reference values of Table 2. PIL= porous insulating layer, PRL= porous reacting layer.

We define $\lambda_{k,PRL}$ as the *relative ability* of the *PRL* to support the respective cathodic reactions. It is a measure that compares the *extent of* the reduction reaction of a species k within the *PRL* to the same activity of k on the metal surface [10]. The extent $\lambda_{k,PRL}$ depends on the *intrinsic ability* of the metal and *PRL* surfaces to support the cathodic reactions, and a host of other variables. Recall that the *intrinsic ability* is the ratio of the exchange current density for the reduction reaction of a species k within the *PRL* to the exchange current density of the same reaction on the metal surface. Using a reduced coordinate, $\xi = x/\delta_f$, the extent $\lambda_{k,PRL}$ thus becomes:

$$\lambda_{k,PRL} = \frac{\int_{\xi=0}^{\xi=1} \left(j_{k,c}\right)_{PRL} d\xi}{\left(j_{k,c}\right)_m} \; ; k \in \{H^+; H_2O; H_2S\} \tag{8}$$

The effect of porosity on the extent $\lambda_{k,PRL}$ for each reduction reaction within the *PRL* is shown in **Figure 8**. For both H_2O and $H_2S_{(aq)}$, the λ_k profiles are almost straight horizontal lines, thus indicating a marginal effect of porosity on the relative ability of the *PRL* surface to support the respective reduction reactions of these two oxidizing species. Also, the value of $\lambda_{k,PRL}$ (~1) suggests that, in absence of internal mass-transport limitations, the two types of surfaces (metal; *PRL*) have an equivalent ability of support for H_2O and $H_2S_{(aq)}$, so that their respective reduction reactions would proceed on either of the two surfaces with no particular preference. As a consequence, no spatial separation of either reaction is, *a fortiori,* expected. In clear contrast to H_2O and $H_2S_{(aq)}$, densification of the porous layer is shown to promote the extent of protons reduction within the *PRL*. Also, the values of $\lambda_{k,PRL}$ (>1) suggest that H^+ reduction would preferentially proceed within the porous reacting layer.

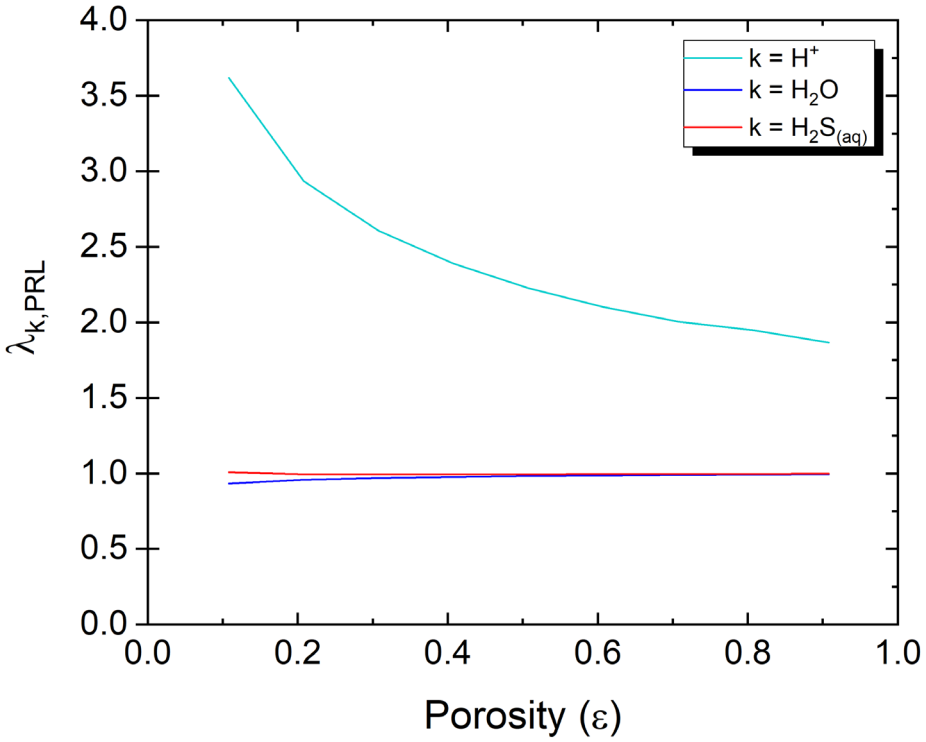

Figure 8. Predicted variations of the extent $\lambda_{k,PRL}$ with porosity at the reference values of Table 2.

CONCLUSIONS

A one-dimensional steady-state model for sour corrosion under a porous Fe_mS_n layer has been developed. The model predictions showed that the oxidizing species, mainly H^+ and $H_2S(aq)$, are progressively depleted within the porous reacting Fe_mS_n layer, thus yielding a progressive delocalization of the cathodic activity towards the boldly exposed surface. The simulation results also show that iron dissolution is even more exacerbated in the presence of active Fe_mS_n layers. When contrasted with inert deposits, the production of HS^-, arising mainly from the direct reduction of $H_2S(aq)$, is more effective when active films are present due to a larger surface area available for the cathodic reduction of $H_2S(aq)$. This would in principle augur a direct consequence on Fe_mS_n precipitation when considering the [H+, HS-] route - based solubility limit, as well as on the film growth. Another important and non-intuitive feature evidenced by the model predictions for active Fe_mS_n layer, and which is worth highlighting, is the existence of a critical porosity. The corrosion rate was indeed found to increase with porosity till the latter reaches a critical value. Further increase of the porosity beyond this critical value was shown to yield a decline of the corrosion rate. The existence of this critical porosity, corresponding to a maximum of the corrosion rate, stems from the counteracting actions of mass transport and cathodic activity (active specific area). A different behaviour was however found in the presence of inert deposits, where the corrosion rate was shown to increase very slightly with porosity. Validation of the model output should be done by contrasting predictions with experimental and field data over an appreciable range of operating conditions.

Although preliminary and in its one-dimension version, the model presented here has been shown to be useful for predicting the coupling behaviour between the steel surfaces and porous reacting layers of iron sulfide. The modelling study has indeed demonstrated that the electrochemical and galvanic activity of iron sulfides on steel can play a significant, in some cases predominant, role in the development of severe sour corrosion attacks. The present effort also paves the way for the development of time-dependent models at higher dimensions (i.e., 2D, 3D) to address the lateral effects and spread of localized attacks, as well as Fe_mS_n precipitation and dissolution.

ACKNOWLEDGMENTS

The authors wish to thank sponsors of the Kjeller Localized Internal Corrosion project for permission to publish the results: BG Group, ConocoPhillips, ExxonMobil, Shell, Total, Clariant, BakerHughes, Nalco, and the Research Council of Norway (contract no. 228222/E30).

.

LIST OF SYMBOLS

C_i	Concentration, $mol.m^{-3}$	$T_{k=K,C}$	Temperature, ^oK (resp. ^oC)
CR	Corrosion rate, $mm.yr^{-1}$	x	Axial coordinate, m
D_i	Diffusion coefficient, $m^2.s^{-2}$	z_i	Valency of species i
E_{corr}	Corrosion potential, V	α	Bruggeman exponent
$E_{eq,k}$	Equilibrium potential for reaction k, V	δ_d	Thickness of the diffusion layer, m
F	Faraday's constant, $96\ 485\ C.mol^{-1}$	δ_f	Thickness of the porous layer, m
f_r	Roughness factor	ε	Porosity
j_k	Current densities, $A.m^{-2}$	φ_e	Electrolyte potential, V
$j_{k,av}$	Average superficial cd, $A.m^{-2}$	φ_s	Solid phase potential, V
$j_{k,c}$	Local cd due to cath. reaction k, $A.m^{-2}$	$\lambda_{k,PRL}$	Extent of support
$j_{k,v}$	Local volume average cd, $A.m^{-3}$	ν_{ik}	Stoichiometric coefficient

$j_{T,av}$	Total average superficial cd, $A.m^{-2}$	Ω_{rpm}	Rotation speed, *rpm*
$j_{T,c}$	Total cathodic cd, $A.m^{-2}$	τ	Tortuosity factor
$j_{T,m}$	Total cathodic cd on metal, $A.m^{-2}$		
N_i	Molar flux, $mol.m^{-2}.s^{-1}$		
n_k	Number of electrons		
N_{mac}	MacMullin number		
NR	Number of cathodic reactions		
PIL	Porous insulating layer		
PRL	Porous reacting layer		
R	Gas constant, $8.314\ J.mol^{-1}.K^{-1}$		
R_i	Homogeneous react. rate, $mol.m^{-3}.s^{-1}$		
R_i'	Electrochem. react. rate, $mol.m^{-3}.s^{-1}$		
$S_{k=a,m}$	Specific surface area, m^{-1}		

REFERENCES

1. C.M. Menendez, et al., «Assessment of Corrosion Under Iron Sulfide Deposits and CO_2/H_2S Conditions», *Corrosion* 69 (2013): p. 145.

2. J.L. Crolet, «Mechanisms of uniform corrosion under corrosion deposits», *Journal of Materials Science* 28 (1993): pp. 2589-2606.

3. J. Kvarekvål and G. Svenningsen, «Effect of Iron Sulfide Deposits on Sour Corrosion of Carbon Steel», CORROSION 2016, paper no. 7313 (Vancouver, CA: NACE, 2016).

4. J. Kvarekvål, «MORPHOLOGY OF LOCALISED CORROSION ATTACKS IN SOUR ENVIRONMENTS», CORROSION 2007, paper no. 7659 (Nashville, TN: NACE, 2007).

5. M. Tjelta and J. Kvarekvål, «Electrochemistry of Mackinawite Electrodes in Sour Aqueous Solutions», CORROSION 2017, paper no. 9319 (New Orleans, LA: NACE, 2017).

6. L.G. Austin and H. Lerner, «THE MODE OF OPERATION OF POROUS DIFFUSION ELECTRODES-I. SIMPLE REDOX SYSTEMS», *Journal of Electrochimica Acta* 9 (1964): pp. 1469-1481.

7. W.E. Ryan, et al., «A Mathematical Model for the Initial Corrosion Rate of a Porous Layer on a Rotating Disk Electrode», *Journal of Electrochemical Scociety* 134 (1987): pp. 2154-2159.

8. F. King, et al., « Modelling the effects of porous layers on corrosion processes», CORROSION 1996, paper no. 380 (NACE, 1996).

9. T.I. Evans and R.E. White, «A Mathematical Model of a Zinc/Bromine Flow Cell», *Journal of Electrochemical Scociety* 134 (1987): pp. 866-874.

10. M.S. Venkatraman, et al., « Corrosion under a porous layer: A porous electrode model and its implications for self-repair», *Journal of Electrochimica Acta* 56 (2011): pp. 8192-8203.